REPORT DOCUMENTATION PAGE

Form Approved OMB NO. 0704-0188

The public reporting burden for this collection of information is estimated to average 1 hour per response, including the time for reviewing instructions, searching existing data sources, gathering and maintaining the data needed, and completing and reviewing the collection of information. Send comments regarding this burden estimate or any other aspect of this collection of information, including suggesstions for reducing this burden, to Washington Headquarters Services, Directorate for Information Operations and Reports, 1215 Jefferson Davis Highway, Suite 1204, Arlington VA, 22202-4302. Respondents should be aware that notwithstanding any other provision of law, no person shall be subject to any oenalty for failing to comply with a collection of information if it does not display a currently valid OMB control number.
PLEASE DO NOT RETURN YOUR FORM TO THE ABOVE ADDRESS.

1. REPORT DATE (DD-MM-YYYY)	2. REPORT TYPE	3. DATES COVERED (From - To)
01-09-2015	MS Thesis	-

4. TITLE AND SUBTITLE
Surface Plasmon Based Engineering of Semiconductor Nanowire Optics

5a. CONTRACT NUMBER
W911NF-11-1-0024

5b. GRANT NUMBER

5c. PROGRAM ELEMENT NUMBER
611103

6. AUTHORS
Carlos Octavio Aspetti

5d. PROJECT NUMBER

5e. TASK NUMBER

5f. WORK UNIT NUMBER

7. PERFORMING ORGANIZATION NAMES AND ADDRESSES
University of California - Irvine
Sponsored Project Administration
5171 California Avenue Suite 150
Irvine, CA 92697 -7600

8. PERFORMING ORGANIZATION REPORT NUMBER

9. SPONSORING/MONITORING AGENCY NAME(S) AND ADDRESS (ES)
U.S. Army Research Office
P.O. Box 12211
Research Triangle Park, NC 27709-2211

10. SPONSOR/MONITOR'S ACRONYM(S)
ARO

11. SPONSOR/MONITOR'S REPORT NUMBER(S)
58162-EL-MUR.95

12. DISTRIBUTION AVAILIBILITY STATEMENT
Approved for public release; distribution is unlimited.

13. SUPPLEMENTARY NOTES
The views, opinions and/or findings contained in this report are those of the author(s) and should not contrued as an official Department of the Army position, policy or decision, unless so designated by other documentation.

14. ABSTRACT
Semiconductor nanowires combine the material properties of semiconductors, which are ubiquitous in modern technology, with nanoscale dimensions and as such, are firmly poised at the forefront of nanotechnology research. The rich physics of semiconductor nanowire optics, in particular, arises from the increased interaction between light and matter that occurs when light is confined to dimensions below the size of its wavelength, in other words, when the nanowire serves as a light trapping optical cavity, which itself is also a source of light. Light confinement is taken to new extremes by coupling to the surface plasmon modes of metallic nanostructures, where light acquires

15. SUBJECT TERMS
plasmon, semiconductor, nanowire optics

16. SECURITY CLASSIFICATION OF:			17. LIMITATION OF ABSTRACT	15. NUMBER OF PAGES	19a. NAME OF RESPONSIBLE PERSON
a. REPORT	b. ABSTRACT	c. THIS PAGE			Peter Burke
UU	UU	UU	UU		19b. TELEPHONE NUMBER 949-824-9326

Report Title

Surface Plasmon Based Engineering of Semiconductor Nanowire Optics

ABSTRACT

Semiconductor nanowires combine the material properties of semiconductors, which are ubiquitous in modern technology, with nanoscale dimensions and as such, are firmly poised at the forefront of nanotechnology research. The rich physics of semiconductor nanowire optics, in particular, arises from the increased interaction between light and matter that occurs when light is confined to dimensions below the size of its wavelength, in other words, when the nanowire serves as a light trapping optical cavity, which itself is also a source of light. Light confinement is taken to new extremes by coupling to the surface plasmon modes of metallic nanostructures, where light acquires mixed photonic and electronic character, and which may focus light to deep-subwavelength regions amenable to the dimensions of the electron wave. This thesis examines how the integration of "plasmonic optical cavities" and semiconductor nanowires leads to substantial modification (and enhancement) of the optical properties of the same, resulting in orders-of-magnitude faster and more efficient light emission with colors that may be tuned as a function of optical cavity geometry. Furthermore, this method is applied to nanowires composed of both direct and indirect bandgap semiconductor materials resulting in applications such as light emission from high-energy states in light emitting materials, highly enhanced broadband light emission from nominally non-light emitting (dark) materials, and broadband (and anomalous) enhancement of light absorption in various materials, all the while maintaining the unifying theme of employing integrated plasmonic-semiconductor optical cavities to achieve tailored optical properties. We begin with a review of the electromagnetic properties of optical cavities, surface plasmon-enhanced light emission in semiconductors, and the key physical properties of semiconductor nanowires. It goes without saying that this thesis work resides at the interface between optical physics and materials science

SURFACE PLASMON BASED ENGINEERING OF SEMICONDUCTOR NANOWIRE OPTICS

Carlos Octavio Aspetti

A DISSERTATION

in

Materials Science and Engineering

Presented to the Faculties of the University of Pennsylvania

in

Partial Fulfillment of the Requirements for the

Degree of Doctor of Philosophy

2014

Supervisor of Dissertation

_____

Ritesh Agarwal, PhD
Professor of Materials Science and Engineering

Graduate Group Chairperson

_____

Shu Yang, PhD, Professor of Materials Science and Engineering

Dissertation Committee

Russell Composto, PhD, Professor of Materials Science and Engineering

Nader Engheta, PhD, H. Nedwill Ramsey Professor of Electrical and Systems Engineering, Bioengineering, and Physics and Astronomy

Ertugrul Cubukcu, PhD, Assistant Professor of Materials Science and Engineering

SURFACE PLASMON BASED ENGINEERING OF SEMICONDUCTOR NANOWIRE OPTICS

Carlos Octavio Aspetti

A DISSERTATION

in

Materials Science and Engineering

Presented to the Faculties of the University of Pennsylvania

in

Partial Fulfillment of the Requirements for the

Degree of Doctor of Philosophy

2014

Supervisor of Dissertation

_____

Ritesh Agarwal, PhD
Professor of Materials Science and Engineering

Graduate Group Chairperson

_____

Shu Yang, PhD, Professor of Materials Science and Engineering

Dissertation Committee

Russell Composto, PhD, Professor of Materials Science and Engineering

Nader Engheta, PhD, H. Nedwill Ramsey Professor of Electrical and Systems Engineering, Bioengineering, and Physics and Astronomy

Ertugrul Cubukcu, PhD, Assistant Professor of Materials Science and Engineering

UMI Number: 3670871

All rights reserved

INFORMATION TO ALL USERS
The quality of this reproduction is dependent upon the quality of the copy submitted.

In the unlikely event that the author did not send a complete manuscript
and there are missing pages, these will be noted. Also, if material had to be removed,
a note will indicate the deletion.

UMI 3670871
Published by ProQuest LLC (2015). Copyright in the Dissertation held by the Author.
Microform Edition © ProQuest LLC.
All rights reserved. This work is protected against
unauthorized copying under Title 17, United States Code

ProQuest LLC.
789 East Eisenhower Parkway
P.O. Box 1346
Ann Arbor, MI 48106 - 1346

SURFACE PLASMON BASED ENGINEERING OF SEMICONDUCTOR

NANOWIRE OPTICS

COPYRIGHT

2014

Carlos Octavio Aspetti

This work is licensed under the
Creative Commons Attribution-
NonCommercial-ShareAlike 3.0
License

To view a copy of this license, visit

http://creativecommons.org/licenses/by-ny-sa/2.0/

My dreams, now realized, are carved on the many sacrifices made by my mother and father, Nelly Aspetti and Herman Aspetti. This is for them.

ACKNOWLEDGEMENTS

I would like to thank the members (past and present) of the Agarwal group who have made these past five years, a transformative experience. My early mentors, Dr. Chang-Hee Cho, Dr. Lambert van Vugt and Dr. Brian Piccione, aided my study of optics while Dr. Sung-Wook Nam introduced me to microfabrication techniques. My many scientific discussions with Pavan Nukala (master of all) were invaluable. Rahul Agarwal and Pavan also provided top quality insight and support in materials characterization. I must also thank Jacob Berger, Joohee Park, Daksh Agarwal, Wenjing Liu, and Karthik Kumar whose capacity for research and success in the lab has been a constant source of inspiration. Dr. Moon-Hyung Jang, Dr. Bumsu Lee, Dr. Liaoxin Sun, Dr. Ming-Liang Ren, Dr. Sajal Dhara, and Dr. Chris Rodd have also provided valuable support in a variety of topics. Last, and certainly not least, I thank my advisor, Prof. Ritesh Agarwal, for believing that I could do this. He treated me as a colleague since day one and I have been hard pressed to find a more potent source of motivation. Everyone had the patience to field my never-ending questions with a smile. Thank you.

I must also thank my PhD cohort, Kate Murphy, Michael O'Reilly, Lisa Chen, Vicky Doan-Nguyen, Pavan Nukala, and Robert Ferrier who were all a constant source of support. Thank you Robert for a decade of camaraderie as we survived the first-ever Physics/Materials Science BS/MS program at Drexel, a PhD program at Penn, and the many trials and tribulations therein. You are my colleague, my friend, and I will not forget you. There are undoubtedly many others who aided in the production of this document and whom I have not named here for the sake of brevity. Know that you are in my thoughts.

ABSTRACT

SURFACE PLASMON BASED ENGINEERING OF SEMICONDUCTOR NANOWIRE OPTICS

Carlos Octavio Aspetti

Ritesh Agarwal, PhD

Semiconductor nanowires combine the material properties of semiconductors, which are ubiquitous in modern technology, with nanoscale dimensions and as such, are firmly poised at the forefront of nanotechnology research. The rich physics of semiconductor nanowire optics, in particular, arises from the increased interaction between light and matter that occurs when light is confined to dimensions below the size of its wavelength, in other words, when the nanowire serves as a light trapping optical cavity, which itself is also a source of light. Light confinement is taken to new extremes by coupling to the surface plasmon modes of metallic nanostructures, where light acquires mixed photonic and electronic character, and which may focus light to deep-subwavelength regions amenable to the dimensions of the electron wave. This thesis examines how the integration of "plasmonic optical cavities" and semiconductor nanowires leads to substantial modification (and enhancement) of the optical properties of the same, resulting in orders-of-magnitude faster and more efficient light emission with colors that may be tuned as a function of optical cavity geometry. Furthermore, this method is applied to nanowires composed of both direct and indirect bandgap semiconductor materials resulting in applications such as light emission from high-energy states in light emitting materials, highly enhanced broadband light emission from nominally non-light

emitting (dark) materials, and broadband (and anomalous) enhancement of light absorption in various materials, all the while maintaining the unifying theme of employing integrated plasmonic-semiconductor optical cavities to achieve tailored optical properties. We begin with a review of the electromagnetic properties of optical cavities, surface plasmon-enhanced light emission in semiconductors, and the key physical properties of semiconductor nanowires. It goes without saying that this thesis work resides at the interface between optical physics and materials science.

TABLE OF CONTENTS

LIST OF ILLUSTRATIONS

diameter demonstrating lasing in plasmonically-coupled CdS below the photonic lasing cutoff. d) Purcell enhancement for plasmonically-coupled CdS. [Adapted from Reference 30].

Figure 2.1 | Schematic of VLS process described in three steps. a) Precursor (PC) comes into contact with catalyst particle above the eutectic temperature. b) Fictitious binary phase diagram demonstrating supersaturation of catalyst with time. c) Solid precursor is precipitated at the catalyst-substrate interface leading to vertical nanowire growth.

Figure 2.2 | a) SEM micrograph of nanowire growth substrate (1 micron scale bar), (inset: tip of nanowire and catalyst particle, 100 nm scale bar). b) SEM micrograph of individual nanowire on substrate used for optical measurement. c) X-ray diffraction data for CdS nanowire growth substrate in (a).

Figure 2.3 | a) Schematic of experimental setup involving pumping of CdS nanowire above the band-gap and both body and end-emission. b) Optical image of nanowire on measurement substrate. c) Same nanowire as (a) under laser excitation.

Figure 2.4 | Optical and morphological properties of VLS grown CdS nanowires. a) Photoluminescence spectrum of unpassivated CdS nanowire (red curve) and SiO_2-passivated CdS nanowire (blue curve). b) Transmission electron microscope micrograph of CdS nanowire coated with 5 nm of SiO_2 (top panel) and FTIR spectrum of uncoated CdS nanowire (bottom panel, black curve) and passivated nanowire (bottom panel, blue curve).

Figure 3.1 | Schematic of E vs. k dispersion relation for an exciton in CdS, depicting the exciton generation, relaxation, and emission process (dark blue curve). E_L denotes the laser excitation energy.

Figure 3.2 | Characterization of core-shell; CdS-SiO_2-Ag nanowire. a) Schematic of core-shell structure. b) TEM micrograph of ALD deposited SiO_2 passivation layer. c) TEM micrograph of 15 nm polycrystalline Ag coating. d) EDX elemental maps demonstrating conformal coatings of all species.

Figure 3.3 | a) Photoluminescence measurements at 77 K for metal-coated (magenta) and bare (blue) nanowires. b) Photoluminescence for metal-coated nanowires with different core diameters (legend: core nanowire diameter).

Figure 3.4 | Comparison between photoluminescence spectra of bare and passivated CdS nanowire (blue curve) and metal-coated CdS nanowire (red curve), both with diameter, d=60 nm. In order to provide a fair comparison of the photoluminescence intensities, we take into account both in-coupling and out-coupling through the thin silver film with respect to the bare nanowire. These were calculated to be 280% (enhancement) of the in-coupling and 5% (reduction) in out-coupling using Lumerical, a commercial Finite Difference Time Domain solver. Overall, a significant (~10x) increase in photon counts is observed for the metal-coated nanowire. The in-coupling enhancement is due to antenna effects whereas the decrease in out-coupling is due to ohmic losses.

Figure 3.5 | a) Schematic of exciton generation, relaxation, and emission process for a thermalized exciton (blue curve, left) and non-thermalized (hot)-exciton (green curve, right) in CdS. E_L denotes the laser excitation energy. b) Photoluminescence spectra associated with the diagram in (a) (also plotted in figure 3.4) and following the same color code for a bare CdS nanowire (blue curve, bottom) and plasmonic-core shell CdS nanowire (green curve, top). The bare CdS nanowire shows emission from thermalized excitons while the metal-coated CdS nanowire cavity shows emission peaks corresponding to non-thermalized (hot) excitons.

Figure 3.6 | Polarization dependence of the photoluminescence intensity as function of angle, θ, from nanowire long-axis, taken by placing a linear polarizer in front of the spectrometer for a) bare nanowire and b) metal-coated nanowire. From the polarization of the A-exciton in figure 3.6a (which is polarized perpendicular to the c-axis of CdS) it is determined that this batch of nanowires is grown with c-axis ~55° (dashed line at bottom of polar plots) from the nanowire long axis (horizontal purple line at bottom of polar plots).

Figure 3.7 | Schematic of naming convention for semiconductor nanowire electromagnetic modes. The black arrows correspond to the electric field polarization with reference to the nanowire below (colored red).

Figure 3.8 | Calculated magnetic field intensity at 2.556 eV (4-LO hot excition/B-exciton energy) for a) d=140 nm plasmonically-coupled nanowire and b) d=140 nm bare nanowire. No electromagnetic mode is observed in the bare nanowire in this energy range. White lines denote material boundaries.

Figure 3.9 | Size-dependent photoluminescence spectra and simulation from plasmonically-coupled core-shell CdS nanowires. a) Size-dependent enhancement of 4-LO hot photoluminescence peak (open circles) and calculated field intensity per unit area (red curve) as a function of nanowire diameter. b-d) Simulated magnetic field (H^2) and electric field (E^2) intensity profiles, as a function of nanowire diameter for three resonant sizes b) d=60 nm (azimuthal mode number, m=2) c) d=100 nm (m=3), and d) d=135 nm (m=4).

Figure 3.10 | a) Time resolved PL spectral map from ensemble of 300-500 nanowires with average diameter 140±50 nm at room temperature (300 K). b) Time-resolved integrated emission intensity for plasmonic (upper) and photonic (lower) nanowires. Solid lines are an exponential fit to the data. Resulting radiative recombination lifetimes of 7 ps and 1600 ps for plasmonically-coupled and bare nanowires respectively are included next to the fitted curves.

Figure 3.11 | Experimentally obtained refractive index values for a) CdSe and b) Ge. The real part of the refractive index (blue curves) and imaginary part (magenta curves) are listed for the wavelength range over which absorption spectra were computed.

Figure 3.12 | Enhanced absorption with anomalous polarization dependence (with respect to a bare CdSe nanowire) in a plasmonically-coupled CdSe nanowire. a, b) Absorption

to dimensions that are resonant with the cavity modes (blue curve). The high efficiency emission channels are labeled A, B, and C from high to low energy. b) Size-dependent photoluminescence spectra of Ω-cavity Si. The white dash lines represent selected off-resonance simulated cavity spectra taken from (c). The yellow dash lines represent resonant simulated cavity spectra corresponding to the experimentally measured size (d=70 and d=55 nm) and are also plotted in (c). c) Simulated spectra of cavity modes at various nanowire diameters in the range d=40 nm-80 nm. The white dash lines correspond to locations of the hot photoluminescence bands.

Figure 4.6 | Simulated cavity mode spectra of resonant-sized cavity (d=70 nm). a-c) Frequency domain profiles of the electric field intensity (log scale) of resonant peaks at a) 2.505 eV, b) 2.342 eV, and c) 2.179 eV respectively. d) Simulated field profile along the Si wire axis (corresponding to 2.505 eV, m=5 mode). The field profile is taken 15 nm below the top surface in the antinode regions of the electric field. The decay length is estimated to be ~200 nm.

Figure 4.7 | a) Photoluminescence spectrum of resonant (d=70 nm) Ω-cavity Si for perpendicular and parallel polarizations (with respect to the nanowire long axis). Numbers 1-5 represent different phonon-mediated hot photoluminescence events. b) Photoluminescence spectrum for non-resonant (d=50 nm) cavity also for perpendicular and parallel polarizations. The perpendicular polarization reveals both cavity, "C", modes and hot photoluminescence, "P", modes. The cavity modes are confirmed by the simulated spectrum of the cavity electromagnetic modes.

Figure 4.8 | a) Phonon dispersion of crystalline Si (adapted from Wei et.al.[20]) The dashed vertical lines indicate phonon modes in high density-of-states (~zero slope) regions. Electronic dispersion of Si (adapted from Chelikowsky et. al.[22]), where dashed lines demonstrate the corresponding electronic states at the same momentum values as high-DOS phonons from a). a) and b) are used to explain the hot photoluminescence bands.

Figure 4.9 | Spontaneous emission enhancement as function energy mismatch between Ω-cavity mode and phonon-mediated hot photoluminescence state for a) resonant size nanowire (d=70 nm) and b) non-resonant size nanowire (d=50 nm). The vertical dash lines represent the positions of the hot photoluminescence bands reported in Figure 4.7a and intersect with the curve corresponding to spontaneous emission enhancement of those states.

Figure 5.1 | a) Schematic of silicon nanowire integrated with a 300 nm thick silver film to form a plasmonic nanocavity (drawn to scale). The native oxide of silicon (SiO_x) is used to separate the active silicon core from the silver shell. b) Scanning electron microscope (SEM) of silver coated silicon nanowire. c) Transmission electron microscope (TEM) image of a representative bare silicon nanowire demonstrating 1.5-2.5 nm of native oxide (denoted by dashed white lines) on the nanowire surface. d) Frequency domain spatial distribution of the electric field intensity in Ω-cavity Si (d=150 nm) demonstrating high order (m=9) mode (obtained via FDTD simulation) and e) corresponding magnetic field intensity.

Figure 5.2 | Photoluminescence spectrum of plasmonically-coupled silicon nanowire (d=150 nm) plotted vs. a) absolute emission energy and b) energy shift from the laser line for various excitation energies in the range 1.959 eV-2.708 eV. Spectra in (b) are plotted with a constant offset of 2×10^3 counts for clarity. The dashed boxes labeled A and B denote high-intensity emission bands. c) Schematic of the electronic dispersion of silicon featuring carrier excitation (magenta arrows), intra-band relaxation and hot-luminescence (green arrows) and radiative recombination from thermalized carriers (blue arrows). This process is examined for relaxation towards the selected conduction band minima at both the X-points (1.12 eV) and L-points (~2.1 eV).

Figure 5.3 | a) Magnified photoluminescence spectra of d=150 nm plasmonically-coupled silicon nanowire in low energy region demonstrating emission below the silicon bandgap at the L-point. (b-e) Variation in spectral positions of subpeaks in photoluminescence spectrum of plasmonically-coupled silicon nanowire. b) variation in band A and c) band B as a function of excitation energy for a single silicon nanowire size (d=150 nm). d) variation in spectral positions of band A and e) band B for several nanowire sizes as a function of excitation energy. Black arrows denotes location of first high intensity peak.

Figure 5.4 | Electromagnetic mode properties of plasmonically-coupled silicon analyzed via FDTD simulations and photoluminescence spectroscopy. a) nomenclature convention for modes polarized parallel (TM) and perpendicular (TE) to the nanowire long-axis. b) Variable-energy excitation photoluminescence spectra of d=150 nm Ω-cavity silicon nanowire juxtaposed with simulated cavity mode spectrum (orange curve). c-f) frequency domain profiles of the electric intensity (log scale) for cavity modes ordered from highest to lowest energy. g) Plot of quality factor versus azimuthal index (m), for TE modes in (b) and represented by the field profiles in (d-f).

Figure 5.5 | a-c) Photoluminescence spectra of plasmonically-coupled nanowires excited at various laser energies in the range 1.959 eV – 2.708 eV for nanowires of size a) d=151 nm, b) d=153 nm, and c) d=156 nm (all spectra are offset by 25,000 counts for clarity). The cavity mode spectrum of the d=151 nm nanowire is plotted on top of the photoluminescence spectra (high in red to low in blue) using the same energy scale. The variable energy excitation photoluminescence spectra demonstrate the role of mode structure in modulating high intensity subpeaks. In addition to size-dependent peak modulation, the modes, which red-shift with increasing size, also enable hot luminescence at lower energies for larger nanowires. d) Photoluminescence spectrum in low energy region (excited with 633 nm, He-Ne laser) for samples (a-c). e) Simulated cavity mode spectra of plasmonically-coupled silicon nanowires with diameters in the range d=150 nm to 160 nm as a function of energy.

Figure 5.6 | a) Temperature dependent photoluminescence spectra of plasmonically-coupled silicon (for two different samples) in the range 77 K-300 K. Increase in overall emission intensity with temperature follows expected trend for hot-luminescence from an indirect bandgap material as the phonon population increases with increasing temperature. b) Plot of total integrated counts as a function of temperature for samples shown in (a).

Figure 5.7 | Difference between the average emission energy and exciting laser energy (i.e. the mean emission shift) plotted against excitation energy. The variation in mean emission energy as function of size and excitation energy highlight the role of both cavity modes and electronic structure in modulating the emission spectrum.

Figure 6.1 | Model of optical refrigeration for a 4-level system. $|0\rangle$ and $|1\rangle$ comprise the electronic states of the ground state manifold separated by energy δE_g. $|2\rangle$ and $|3\rangle$ comprise the excited state manifold separated by energy δE_u. W_{rad} and W_{nr} are the radiative and non-radiative decay rates respectively, while w_1 and w_2 correspond to the phonon-mediated thermalization rate of the ground state and excited state manifolds respectively. [Adapted from reference 10]

Figure 6.2 | Stokes and anti-Stokes Raman scattering for bare CdS nanowire (d~200 nm) with 5 nm conformal SiO_2 coating. a) Raman spectrum featuring broad photoluminescence peak centered at ~1157 cm-1 (2.474 eV) which is attributed to excitonic emission from CdS. b) Magnified view of region near 2LO Raman peaks in both the Stokes and anti Stokes region. Spectra have been baseline corrected to eliminate the photoluminescence background and provide accurate values of the Raman intensity.

Figure 6.3 | Stokes and anti-Stokes Raman scattering for metal coated CdS nanowire with 5 nm conformal SiO_2 coating and 300 nm Ag metal shell (green curves). a) Raman spectrum featuring broad photoluminescence peak centered at ~980 cm^{-1} (2.452 eV) which is attributed to excitonic emission from CdS. The spectrum of a bare (non-metal coated) CdS nanowire is also plotted for comparison (black curve). b) Magnified view of region near 2LO Raman peaks in both the Stokes and anti Stokes region. Spectra have been baseline corrected to eliminate the photoluminescence background and provide accurate values of the Raman intensity.

Figure 6.4 | Atomic force microscopy of CdS nanobelts. a) AFM image of typical thick CdS nanobelt with thickness of ~240 nm. b) AFM profiles of typical thick and thin CdS nanobelts as discussed in section 6.2.

Figure 6.5 | Differential Luminescence Thermometry temperature calibration curve and schematic of measurement scheme. a) Photoluminescence at several times in the range 0-18 minutes for a CdS sample at a fixed temperature of 268 K. The photoluminescence peak position reaches a steady state within ten minutes of stabilization of the sample stage temperature. b) Photoluminescence spectra for a representative CdS samples at various temperatures in the range 268 K to 312 K (plotted at 8 K intervals for clarity). c) Plot of change in temperature, ΔT, vs. change in spectral peak position, ΔE, obtained from the photoluminescence data in (b). The blue line represents a linear fit to the data. d) schematic of measurement process using a pump laser (514.5 nm) for cooling and a low power probe laser (473 nm) for monitoring the shift in the photoluminescence spectrum.

Figure 6.6 | Optical image of CdS nanobelt suspended over PMMA boxes (~9 μm x 9 μm) with a ~4 μm separation. The bright emission from the nanobelt is anti-Stokes photoluminescence resulting from excitation below the bandgap at (with the 514.5 nm pump laser).

Figure 6.7 | Anti Stokes photoluminescence in bare CdS nanobelts with thickness *d*~200-300 nm. a) Photoluminescence in CdS nanobelt excited with the 514.5 nm line of a CW laser (inset: optical image of anti Stokes photoluminescence excited with pump laser). b) Magnified view of anti Stokes photoluminescence spectrum in CdS nanobelt featuring a blue shift of ~1.74 meV (~0.3 nm), which reaches a steady state after 15 minutes of excitation with the pump laser. c) Magnified view of anti Stokes photoluminescence spectrum in CdS nanobelt featuring a blue shift of 2.6 meV (~0.5 nm) after 1 hour of excitation with pump laser.

Figure 6.8 | Pump-probe differential luminescence thermometry of bare and passivated CdS nanobelts. a) Stokes Photoluminescence spectra of a CdS nanobelt featuring the spectrum at time t=0 (black curve) and t=15 min (after pump excitation; red curve). The difference spectrum (DLT curve) is plotted in magenta. c) Stokes Photoluminescence spectra of a CdS nanobelt passivated with SiO_2 featuring the spectrum at time t=0 (black curve) and t=10 min (red curve). The difference spectrum (DLT curve) is also plotted in magenta.

Figure 6.9 | Probe photoluminescence peak position and sample stage temperature vs. time for two bare CdS nanobelt samples in the temperature range a) 307 K-311 K and b) 311 K-316K.

Figure 6.10 | Laser cooling of plasmonically-coupled CdS in geometry optimized for top-down excitation and measurement. a) Schematic of CdS integrated with a 15 nm thick Ag film. Excitation is performed through the Ag film as denoted by the dark green and purple arrows. Emission is also measured through the substrate (bright green arrow). b) Stokes Photoluminescence spectra of a CdS nanobelt featuring the spectrum at time t=0 (black curve) and t=15 min (after pump excitation; red curve). The difference spectrum (DLT curve) is plotted in magenta. c) Magnified view of anti-Stokes photoluminescence (excited with probe laser) of data presented in (b).

Figure 6.11 | Laser cooling of plasmonically-coupled CdS using inverted geometry. a) Schematic of CdS integrated with a 300 nm thick silver film. Excitation is performed through the substrate as denoted by the dark green and purple arrows. Emission is also measured through the substrate (bright green arrow). b-d) Magnified view of Anti-Stokes photoluminescence (excited with probe laser) b) after 10 minutes of cooling, c) after 2 minutes of warm up time (after excitation with pump laser has ceased) and d) 5 minutes of warm up time. The original probe photoluminescence spectrum at t=0 is plotted in black in all three plots as a reference point.

Figure 7.1 | Photoluminescence of plasmonically-coupled Si nanowire (*d*~150 nm) excited with the 457.8 nm laser line of an Argon-ion laser (continuous wave, blue curve) and Ti:Sapphire laser (pulse width 140 fs, 80 MHz repetition rate) tuned to 458 nm (magenta curve).

Chapter 1. Introduction

Reproduced in part with permission from Reports on Progress in Physics, Volume 77, Issue 8, Pages 1-20. Copyright 2014 ACS Publications

Reproduced in part with permission from the Journal of Physical Chemistry Letters (accepted, October 2014)

1.1: Cavity Electromagnetics Primer: Light Emission in Optical Cavities

When we think of optics of materials, we typically recall phenomena such as reflection and refraction, i.e. geometric optics. This is an example of the interaction between light and matter, where light moves the free and bound charges in a material giving rise to all the optical phenomena.[1] Yet, some of the most interesting effects arise when (i) light interacts with active media, that is materials which have electronic resonances in the same spectral range of the incoming light, and (ii) when that light is placed in a light-trapping box. In 1946, Edward Purcell was the first to realize that the rate of light emission from a radiating dipole (such as the electron-hole pair in a semiconductor) is a function of the surroundings of that optical emitter.

Originally developed for radio-frequency operation, the enhanced spontaneous emission rate of the emitter may be expressed as:

$$\gamma = \frac{3Q}{4\pi^2}\left(\frac{\lambda^3}{V_m}\right)\gamma_0 \qquad \text{Eq. 1.1}$$

where γ_0 is the spontaneous emission rate in free space, λ is the wavelength of the emitted radiation in the host medium, Q is the quality factor of the electromagnetic mode that couples to the optical emitter, and V_m is the mode volume of the same.[2] The quality

factor is a measure of the optical cavity to store electromagnetic energy; analogous to how a capacitor stores electrical energy. It can also be considered as a measure of how long light is confined to the optical cavity before leaking into the vacuum. In the denominator we find the mode volume, which can be expressed as:

$$V_m = \frac{\int \varepsilon(r)E^2(r)d^3r}{(\varepsilon(r)E^2(r))_{max}} \qquad \text{Eq. 1.2}$$

where $\varepsilon(r)$ is the dielectric constant of the material and $E^2(r)$ the electric field intensity. This is a measure of the confinement of the electromagnetic field. It has the units of volume and, in fact, is often quoted with respect to the volume taken up by light in free space, λ^3. The enhancement in the spontaneous emission rate, γ/γ_0, is known as the Purcell factor, and depends on the ratio Q/V_m. In other words, in order to obtain highly enhanced spontaneous emission rates, we should place optical emitters in environments that have long lived modes (high Q) and where the optical modes are also highly confined (low V_m). As expected, these two quantities are typically anti-correlated. The smaller the mode volume, the more likely it is that light will leak out (lower Q) and vice versa. Furthermore, there is a fundamental limit on the mode volume of light, known as the diffraction limit, where for example in the case of waveguided modes, light may not be confined to dimensions much smaller than one-half its wavelength in the host medium (this is also known as the "cutoff energy" in the waveguide literature).[3] For completeness's sake, we note that the above expression assumes perfect spectral matching between the emitter and the optical cavity mode. In reality, both spectral overlap as well as spatial and polarization overlap between the optical emitter and

electromagnetic mode must be taken into account for accurate computation of the Purcell factor[4] (see section 4.6). The physical origin of the Purcell effect is rooted in Fermi's golden rule, where the spontaneous emission rate of an optical emitter may be computed as:

$$\gamma = \frac{2\pi}{\hbar}\left|\langle f|\vec{d}\cdot\vec{E}(\vec{r})|i\rangle\right|^2\rho(\hbar\omega) \qquad \text{Eq. 1.3}$$

and where $\langle f|\vec{d}\cdot\vec{E}(\vec{r})|i\rangle$ is the transition dipole matrix element for the transition between state f and state i, and $\rho(\hbar\omega)$ is the photon density of states. Here, the Q/V_m ratio from the Purcell factor in classical terms may be related to the density of photon states, ρ, in the quantum electrodynamics picture. For an insightful derivation of the Purcell effect in terms of classical parameters (as expressed above), but beginning with Fermi's golden rule, the reader is referred to a recent review by Maier et al.[5]

Though it was initially developed for radio-frequency operation, the Purcell effect is a general principle that can be applied across the electromagnetic spectrum. Advances in nanofabrication have enabled the engineering of optical cavities with nanoscale dimensions, thus tuning their resonances to the nanoscale portion of the electromagnetic spectrum (in terms of wavelength), or in other words, the UV-visible-near IR frequencies. This is a boon from the perspective of semiconductor technology as many relevant elemental and compound semiconductors (Ge, Si, InP, GaAs, etc.) feature band gaps and light emission in this spectral range.[6] Implicit here is the fact that the electron-hole pairs of semiconductors may function as optical emitters, the light emission of which may be

tuned as a function of the surroundings. As mentioned above, due to the fundamental limit on the mode volume, and thus the size of the optical cavity, research has focused on optimizing the quality factor of optical cavities.[7,8] Figure 1.1 is a summary of conventional optical cavities, where the light source is a semiconductor quantum dot that is embedded in an optical cavity fabricated via top-down methods.[8] Optical cavities in the Whispering Gallery Mode resonator geometry (where light is confined to the circumference of a circular cavity) excel at hosting high Q modes; 125 being one of the highest Purcell factors achieved at optical frequency with a corresponding quality factor of 12,000.[9] Quality factors as high as 10^8 have been achieved at IR frequency. [10]

Such Purcell enhancement schemes suffer from three main drawbacks. First, as can be observed in figure 1.1, high Q cavities feature large spatial footprints generally of several microns limiting their applicability in nanotechnology. Secondly, in these cases the optical emitter and optical cavity are two separate entities which must be properly aligned to achieve the desired results, and which adds another level of difficulty to their fabrication. Finally, perhaps the most fundamental limitation on these high Q cavities is their limited operational bandwidth. A high quality factor, or long-lived mode in time domain, equates to a narrow peak in frequency space, where the peak width, Δf, is related to the quality factor at the resonance frequency, f_0, as $\Delta f = f_0/Q$. For the previously mentioned high-Q resonator (Q=12,000), this equates to a mode width <1 meV, thereby placing a significant constraint on the operation of this hybrid optical cavity-semiconductor device. If we are only interested in enhancing spontaneous emission, then the best systems would be monolithically integrated optical cavity-

semiconductor hybrid structures, which optimize Q/V_m not just through high Q and low V_m but rather through low Q, which equates to operation over a broad frequency range, and ultralow mode volumes, significantly below the diffraction limit, thereby maintaining the high Q/V_m ratio. Metals excel at confining light into deep-subwavelength dimensions, where light couples to surface modes on the metal surface and acquires both photonic and electronic character. This type of optical mode is termed the "surface plasmon" and will be the focus of the next subsection.

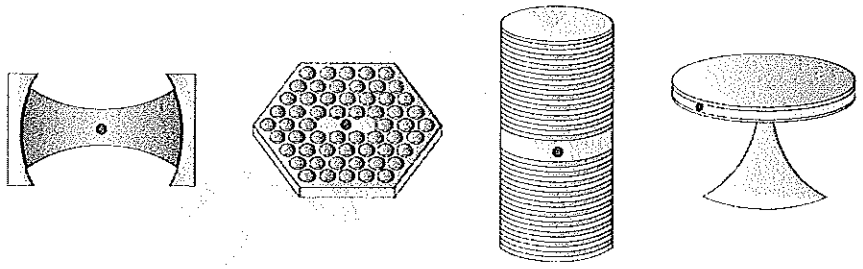

Cavity	Length = 42.2 μm; Width = 23.4 μm;	Photonic crystal slab	Micropillar	Microdisk
λ (nm); E (eV)	852.4; 1.45	1,182; 1.32	937; 1.32	744; 1.66
Q	4.4×10^7	6,000	7,350	12,000
V (μm^3)	$18{,}148 = 3 \times 10^4 (\lambda/n)^3$	$0.04 = (\lambda/n)^3$	$0.3 = 16(\lambda/n)^3$	$0.07 = 8(\lambda/n)^3$
$F_P = \frac{3Q\lambda^3}{4\pi^2 n^3 V}$	114	441	36	125
$\kappa/2\pi$ (GHz)	0.008	42	44	34

Figure 1.1 | Different all-dielectric cavity paradigms and corresponding cavity Quantum Electrodynamics parameters. The red dot corresponds to the position of the optical emitter (quantum dot). For the full figure (including Rabi Splitting magnitude, etc.) please refer to the original review article by Khitrova et. al.[10] [Adapted from Reference 10]

1.2: Surface Plasmons and their Role as Optical Cavities and Antennas

Metals excel at confining light into deep-subwavelength dimensions. When light (photon) is incident on the surface of a metal (in the spectral region where the metal has negative values of permittivity), the surface electrons and photon may form a strongly coupled system, also known as the surface plasmon polariton (SPP).[11] The surface electrons serve to "anchor" the light to the surface of the metal resulting in an electromagnetic mode that may only propagate on the surface of the metal. The SPP features a dispersion relation that is similar in form to that of other strongly coupled systems (such as the exciton-polariton in semiconductors[1]) and which dictates its physical properties. For a detailed description of SPPs the reader is referred to section 1.2.1. In a similar fashion, localized surface plasmons (LSPs) are non-propagating modes, which may be excited in deep-subwavelength structures where the light-matter interaction may be treated quasistatically.[12] Physically speaking, the key difference between SPPs and LSPs is that LSPs are not bound to the same dispersion relation as SPPs, which facilitates their excitation from the far-field[12] (see section 1.2.1). Both are surface plasmon (SP) resonances. Given that ratio of surface to volume increases as the dimensions of the system shrink, at the nanoscale, the optical properties of metals are dominated by SP resonances.

---

[1] For a general overview of strong light-matter coupling and its observation in semiconductors, the reader is referred to C. F. Klinghshirn's "Semiconductor Optics", 3rd ed., Chapters 5 and 6.